

Traversable Wormholes Sourced by Dark Matter in Loop Quantum Cosmology

Marcos V. de S. Silva* and G. Alencar†

*Departamento de Física, Universidade Federal do Ceará,
Caixa Postal 6030, Campus do Pici,
60455-760 Fortaleza, Ceará, Brazil.*

R. M. P. Neves‡ and Celio R. Muniz§

*Universidade Estadual do Ceará (UECE),
Faculdade de Educação, Ciências e Letras de Iguatu,
Av. Dário Rabelo s/n, Iguatu - CE, 63.500-00 - Brazil.*

(Dated: November 20, 2024)

Abstract

In this work, we investigate the existence of wormholes within the framework of Loop Quantum Cosmology, considering isotropic dark matter as the matter source. We examine three distinct density profiles and employ modified field equations along with stress-energy tensor conservation, applying suitable boundary conditions to derive traversable wormhole solutions. We confirm that each obtained solution meets the geometric requirements for wormholes and assess the regularity of these spacetimes by computing the Kretschmann scalar to ensure the absence of singularities. Through the stress-energy tensor, we analyze the conditions under which energy conditions may be violated in this model. We explore the geometry of these wormholes using embedding diagrams, and evaluate the stability of the solutions by examining the speed of sound. Lastly, we compute the amount of exotic matter necessary to sustain these structures using the Volume Integral Quantifier.

Keywords: General Relativity; Loop Quantum Cosmology; Traversable Wormholes; Dark Matter

*Electronic address: marcosvinicius@fisica.ufc.br

†Electronic address: geova@fisica.ufc.br

‡Electronic address: raissa.pimentel@uece.br

§Electronic address: celio.muniz@uece.br

I. INTRODUCTION

General Relativity (GR) has successfully described gravitational phenomena for over a century, providing a robust framework for understanding spacetime curvature as influenced by matter and energy. This theory's predictions, from planetary orbits to black hole properties, have been verified extensively, notably in strong-field regimes with the detection of gravitational waves by LIGO and Virgo collaborations [1]. Another fascinating consequence of GR is the possibility of traversable wormholes, hypothetical passages through spacetime that could connect distant points or even different universes [2–4]. Unlike black holes, which are characterized by an event horizon that prevents anything from escaping, traversable wormholes remain open, allowing for potential passage by particles and light.

However, constructing stable wormhole solutions within GR typically requires exotic matter – substances that violate energy conditions such as the Null Energy Condition (NEC) [5–8]. This need for exotic matter has driven investigations into alternative sources and modifications of GR, particularly in theories that incorporate quantum gravitational effects, such as Loop Quantum Gravity (LQG). Loop Quantum Cosmology (LQC), a simplified model of LQG, introduces corrections to classical GR, especially at high densities, by imposing a critical density ρ_c , beyond which quantum geometric effects become significant [9]. In this sense, traversable wormholes in scenarios of LQC were built in [10, 11]. Such quantum effects hold the potential to reduce or even eliminate the need for exotic matter in sustaining wormholes, allowing other forms of matter, such as dark matter, to support their structure.

The enigmatic nature of dark matter remains one of physics' greatest puzzles, thought to comprise around five-sixths of the universe's matter [12]. Its presence is strongly supported by astrophysical observations, such as galaxy rotation curves that indicate more mass than visible matter alone can explain [13–16]. Dark matter's mass scale, spanning from cosmic structures down to 10^{-22} eV, is still undetermined, making the identification of its particle nature a priority in modern physics [17]. One theory suggests that primordial black holes, originating shortly after the Big Bang, might serve as dark matter. Another possibility involves new particles beyond the Standard Model, like axions and Weakly Interacting Massive Particles (WIMPs), which might accumulate and annihilate in the Sun, emitting neutrinos detectable by observatories like IceCube, though no confirmation has yet been found [18, 19]. It is worth noting that dark matter as a source of wormholes was

investigated in several papers, in Einstein and modified gravity [20–26].

In this work, we explore the existence of traversable wormholes sourced by isotropic dark matter within the framework of LQC. We investigate three cold dark matter models – Navarro-Frenk-White (NFW), Pseudo-Isothermal (PI), and Perfect Fluid (PF) models [27, 30] – each with distinct density profiles that influence the stability and structure of wormhole solutions. While in the context of General Relativity dark matter does not possess an exotic nature, it may exhibit such characteristics within certain modified gravity frameworks. Then we adopt a linear equation of state, $p = \omega\rho$, where ω can potentially take on negative values. Thus, by employing the LQC-modified Einstein and conservation equations with linear EoS, we derive shape and redshift functions for each dark matter model to assess whether the resulting geometries satisfy the conditions for traversable wormholes, such as the flaring-out condition and asymptotic flatness. Following, we examine the regularity conditions of the corresponding spacetimes by computing the Kretschmann scalar. We further examine energy conditions by analyzing the effective stress-energy tensor derived from the dark matter density profiles, noting that the violation of NEC may vary with the choice of model and parameters, particularly ρ_c and ρ_0 , the LQC critical density and central density of dark matter, respectively.

Through embedding diagrams, we visually represent the wormhole shapes for each model, illustrating how changes in the parameters influence their structure. Furthermore, by calculating the Volume Integral Quantifier (VIQ), we evaluate the amount of exotic matter required to sustain each wormhole, comparing the models between themselves. The stability of these wormholes is also analyzed through sound speed calculations within the employed isotropic dark matter fluids. This work underscores, therefore, the role of quantum corrections from LQC in potentially creating stable, traversable wormholes sustained by dark matter, advancing the study of non-classical spacetimes as viable exotic structures within modified gravity theories.

The structure of this paper is as follows: In Section II, we introduce the dark matter models to be used and the modified Einstein equations for general traversable wormhole solutions in the context of LQC. In Sections III, IV, and V, we derive these wormhole solutions for the three dark matter models and discuss their geometric properties. Section VI explores the embedding diagrams of the obtained wormhole solutions. In Section VII, we examine the energy conditions and calculate the necessary amount of exotic matter. In

Section VIII, we analyze the stability of the solutions by investigating the sound velocity within the isotropic fluid. Finally, Section IX presents the conclusions and closes the paper.

Throughout this paper, we utilize natural units with $8\pi G = c = 1$ and adopt the metric signature $(-, +, +, +)$.

II. DARK MATTER MODELS AND LQC-INSPIRED WORMHOLES

We will work with the cold dark matter models whose density profiles can be synthesized in the following formula:

$$\rho(r) = \frac{\rho_0}{\sum_{n=0}^3 a_n (r/R_s)^n}, \quad (1)$$

where R_s and ρ_0 are a distance scale and a density parameter, respectively, which are associated with the dark matter distribution. The coefficients a_n depends on the model under analysis. Thus, we have

$$\text{NFW: } a_0 = 0, a_1 = 1, a_2 = 2, a_3 = 1; \quad (2)$$

$$\text{PI: } a_0 = 1, a_1 = 0, a_2 = 1, a_3 = 0; \quad (3)$$

$$\text{PF: } a_0 = a_1 = a_2 = 0, a_3 = 1, \quad (4)$$

where NFW stands for Navarro-Frenk-White, PI is for Pseudo-Isothermal, and PF denotes Perfect Fluid model. A plausible justification for using these dark matter profiles as sources for wormholes in the context of LQC lies in their distinct structural characteristics, which offer a range of gravitational behaviors under some density conditions near the wormhole throat. The NFW profile, with its cuspy core, represents a widely observed density distribution in galaxies and clusters, while the pseudo-isothermal model provides a softened central density, helping to capture alternative galactic dynamics. Meanwhile, the PF dark matter model, often applied in theoretical explorations, features an equation of state that supports pressure, making it particularly useful in analyzing exotic configurations like black holes and wormholes [28, 29].

Our exploration of traversable wormholes sourced by dark matter is inspired by principles coming from LQC. The solution arises from an effective matter fluid that simulates corrections within the framework of LQC. Consequently, the effective gravity-matter system obeys the Einstein equations:

$$G^\mu{}_\nu \equiv R^\mu{}_\nu - \frac{1}{2}g^\mu{}_\nu R = T^\mu{}_\nu, \quad (5)$$

where $T_{\mu\nu}$ denotes the effective stress-energy tensor, which is, for an isotropic perfect fluid, given by

$$T_{\nu}^{\mu} = \text{diag}(-\rho_e, p_e, p_e, p_e), \quad (6)$$

where $\rho_e = -G^t_t$, $p_e = G^r_r = G^{\theta}_{\theta} = G^{\phi}_{\phi}$. The analytical expressions for the effective energy density and pressure are given by [10, 11]:

$$\rho_e(r) = \rho \left(1 - \frac{\rho}{\rho_c}\right), \quad (7)$$

$$p_e(r) = p - \rho \left(\frac{2p + \rho}{\rho_c}\right), \quad (8)$$

where ρ_c represents the critical density in the context of LQC.

Therefore, moving forward, we will investigate the wormholes in the context of LQC. We will particularly focus on the energy density given in Eq. (7) by the static and spherically symmetric Morris-Thorne wormhole metric as presented by [3]:

$$ds^2 = -e^{2\Phi(r)} dt^2 + \frac{dr^2}{1 - \frac{b(r)}{r}} + r^2 d\Omega_2. \quad (9)$$

Here, $\Phi(r)$ represents the redshift function, $b(r)$ is the shape function, and $d\Omega_2 = d\theta^2 + \sin^2\theta d\phi^2$ denotes the spherical line element. Given the metric ansatz of Eq. (9), the modified Einstein equations take on their simplest form:

$$G^t_t = \frac{b'}{r^2} = \rho_e(r), \quad (10)$$

$$G^r_r = -\frac{b}{r^3} + 2\frac{(r-b)\Phi'}{r^2} = p_e(r), \quad (11)$$

$$G^{\theta}_{\theta} = G^{\phi}_{\phi} = \left(1 - \frac{b}{r}\right) \left[\Phi'' + (\Phi')^2 + \frac{(b-rb')}{2r(r-b)}\Phi' + \frac{(b-rb')}{2r^2(r-b)} + \frac{\Phi'}{r}\right] = p_e(r), \quad (12)$$

The quantities $\rho(r)$ and $p(r) = \omega\rho(r)$ that entry in the effective densities and pressures are described by Eq. (1), and will be regarded as the sources for the new wormhole solutions investigated here.

Another key feature of the isotropic traversable wormhole solutions to be derived here is that they must satisfy the modified conservation equation:

$$\frac{dp_e}{dr} + \frac{d\Phi}{dr}(\rho_e + p_e) = 0, \quad (13)$$

where we assume identical radial and lateral pressures due to the source isotropy. This equation is inherently satisfied, as the Einstein tensor for any general geometry is divergence-free.

To verify the presence of singularities in these spacetimes, it is important to examine whether there are divergences in the curvature invariants. Since the spacetimes we are dealing with in this work are spherically symmetric, it is sufficient to check the Kretschmann scalar, defined as $K = R^{\mu\nu\alpha\beta}R_{\mu\nu\alpha\beta}$, where $R^{\mu\nu\alpha\beta}$ is the Riemann tensor.

For our shape function to describe traversable wormholes, there are certain conditions it must satisfy. Our solution must have a throat, i.e., a minimum size, should not have event horizons, and the wormhole opening must remain [3] Mathematically, this can be analyzed through the shape function as follows: i) $b(r_0) = r_0$; ii) $b(r) < r$ must be valid for $r > r_0$; iii) $b'(r_0) < 1$; iv) and $b(r) - b'(r)r > 0$.

III. NFW MODEL

A. Shape function

From Eqs. (1), (2), (7), and (10) we find that the corresponding wormhole shape function is given by

$$b(r) = r_0 - \frac{R_s^3 \rho_0}{\rho_c} \left[\frac{\rho_0}{3 \left(1 + \frac{r_0}{R_s}\right)^3} + \frac{\rho_c}{\left(1 + \frac{r_0}{R_s}\right)} \right] + \frac{R_s^3 \rho_0}{\rho_c} \left[\frac{\rho_0}{3 \left(1 + \frac{r}{R_s}\right)^3} + \frac{\rho_c}{\left(1 + \frac{r}{R_s}\right)} \right] + R_s^3 \rho_0 \log \left(\frac{1 + \frac{r}{R_s}}{1 + \frac{r_0}{R_s}} \right), \quad (14)$$

where we have taken into account the boundary condition $b(r_0) = r_0$ in order to determine the integration constant.

The condition $b(r_0) = r_0$ was used to integrate the field equation and obtain the form of $b(r)$. However, we still need to verify whether the other conditions mentioned in the before are also satisfied. In Fig. 1, we observe the behavior of $b(r)/r$ and notice that, for $r > r_0$, the ratio $b(r)/r$ is always less than one, thus satisfying the condition *ii* that we established earlier. In Fig. 2, we analyze the behavior of $b'(r)$ and observe that it is always less than one, ensuring that the condition $b'(r_0) < 1$ is easily satisfied. In Fig. 3, we examine the behavior of the relation $b(r) - rb'(r)$ and observe that it is always positive, ensuring that the flaring condition is always satisfied. Thus, we see that the wormhole model derived from LQC, when considering dark matter described by the NFW profile, satisfies the established conditions.

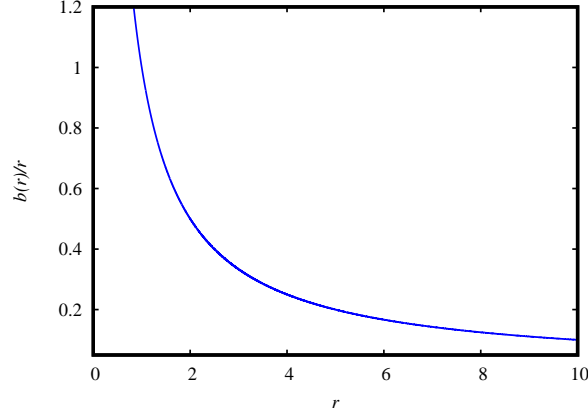


Figure 1: Behavior of $b(r)/r$ considering the model (14) in terms of the radial coordinate with $r_0 = 1$, $R_s = 2$, $\rho_c = 10^{-5}$, and $\rho_0 = 10^{-6}$. Changes in the densities ρ_c and ρ_0 do not significantly alter the shape of the graph.

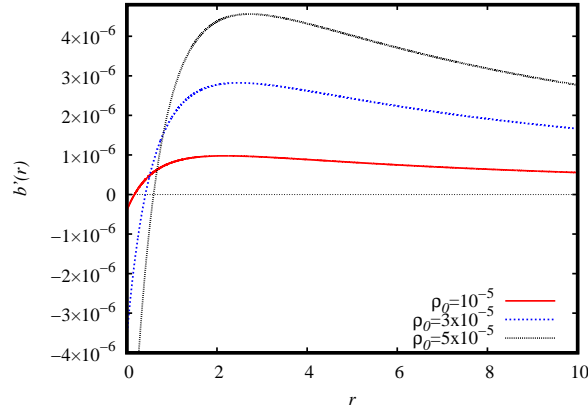


Figure 2: Behavior of $b'(r)$ considering the model (14) in terms of the radial coordinate with $r_0 = 1$, $R_s = 2$, and $\rho_c = 10^{-5}$, for different values of ρ_0 . Changes in the density ρ_c do not significantly alter the shape of the graph.

B. Redshift function

From Eq. (1), (2), (13), and the state equation $p(r) = \omega\rho(r)$, we find

$$e^{2\Phi(r)} = \left(\frac{r}{r_0}\right)^{\frac{2(1+2\omega)}{1+\omega}} \left(\frac{r+R_s}{r_0+R_s}\right)^{\frac{4(1+2\omega)}{1+\omega}} \left[\frac{r_0(r_0+R_s)^2\rho_c - 2R_s^3\rho_0}{r(r+R_s)^2\rho_c - 2R_s^3\rho_0}\right]^2, \quad (15)$$

where we have chosen the integration constant such that, at the throat, $e^{2\Phi(r_0)} = 1$. This metric's time coefficient exhibits an undesirable asymptotic behavior, except when $\omega \rightarrow 0$, thereby necessitating in general the imposition of junction conditions. However, the

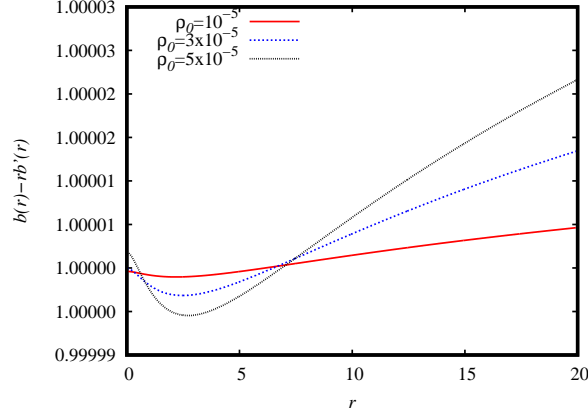


Figure 3: Behavior of $b(r) - rb'(r)$ considering the model (14) in terms of the radial coordinate with $r_0 = 1$, $R_s = 2$, and $\rho_c = 10^{-5}$, for different values of ρ_0 . Changes in the density ρ_c do not significantly alter the shape of the graph.

curvature scalars clearly indicate that asymptotic flatness is in fact achieved, as we will demonstrate. This property holds consistently across all dark matter models.

Once we have the shape function and the redshift function, we are able to obtain the Kretschmann scalar. Analytically, the Kretschmann scalar is quite lengthy and complex, making its information unclear; therefore, we will not include it here. What we can identify is that our spacetime will only be free of singularities for $\rho_0 < \rho_c r_0 (r_0 + R_s)^2 / 2 R_s^3$. Thus, we verify that if the dark matter density is very high, it may end up generating singularities in our spacetime. In Fig. 4, we graphically observe the behavior of the Kretschmann scalar and see that it does not show divergences as it approaches the throat radius, decreasing to zero as the radial coordinate increases. Respecting the regularity condition imposed on the energy density of the dark matter and considering that ρ_c must have small values to deviate from the general relativity results, parameter changes do not significantly alter the behavior of the Kretschmann scalar; therefore, we have not included additional curves in Fig. 4.

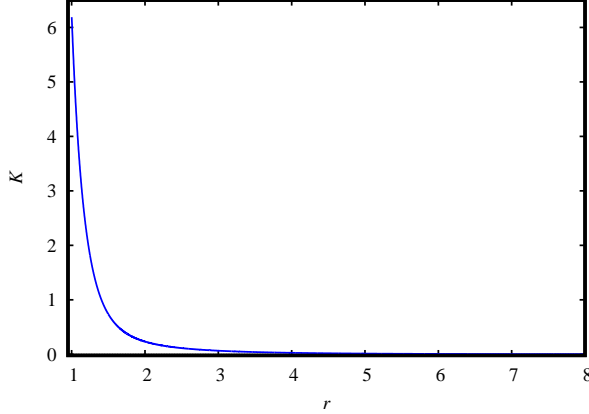


Figure 4: Behavior of the Kretschmann scalar for model (14), as a functions of the radial coordinate, with $\omega = 1$, $r_0 = 1$, $R_s = 2$, $\rho_c = 10^{-5}$, and $\rho_0 = 10^{-6}$.

IV. PI MODEL

A. Shape function

From Eqs. (1), (3), (7), and (10) we find that the corresponding wormhole shape function is given by

$$\begin{aligned}
 b(r) = & r_0 - \rho_0 r_0 R_s^2 - \frac{\rho_0^2 r_0 R_s^4}{2\rho_c} (r_0^2 + R_s^2) + \rho_0 R_s^3 \tan^{-1} \left(\frac{r_0}{R_s} \right) + \frac{\rho_0^2 R_s^3 \tan^{-1} \left(\frac{r_0}{R_s} \right)}{2\rho_c} \\
 & + \rho_0 r R_s^2 + \frac{\rho_0^2 r R_s^4}{2\rho_c (r^2 + R_s^2)} - \frac{\rho_0^2 R_s^3 \tan^{-1} \left(\frac{r}{R_s} \right)}{2\rho_c} - \rho_0 R_s^3 \tan^{-1} \left(\frac{r}{R_s} \right). \quad (16)
 \end{aligned}$$

Let us now verify whether the model satisfies the conditions imposed previously. The condition $b(r_0) = r_0$ is automatically satisfied since this condition was imposed during the integration process to obtain $b(r)$. The second condition, $b(r)/r < 1$ for $r > r_0$, is always satisfied, as we see from Fig. 5 that for model (16) the function $b(r)/r$ is always less than one for $r > r_0$. Through Fig. 6, we see that $b'(r)$ is always less than one, even taking negative values. This shows that the third condition, $b'(r_0) < 1$, is satisfied. Through Fig. 7, we see that $b(r) - b'(r)r > 0$ for model (16), so that the fourth condition is always satisfied. Thus, depending on the chosen parameter values, model (16) meets all the conditions for a wormhole.

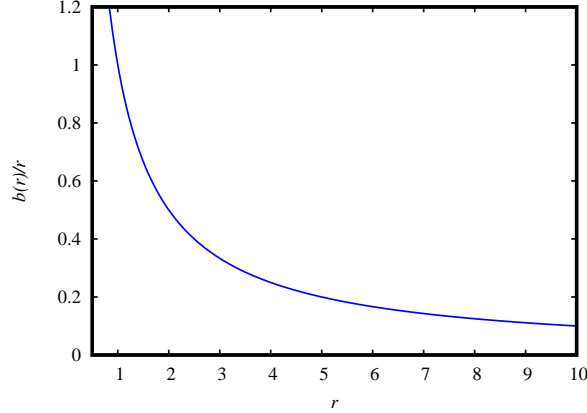


Figure 5: Behavior of $b(r)/r$ considering the model (16) in terms of the radial coordinate with $r_0 = 1$, $R_s = 2$, $\rho_c = 5 \times 10^{-5}$, and $\rho_0 = 10^{-6}$. Changes in the densities ρ_c and ρ_0 do not significantly alter the shape of the graph.

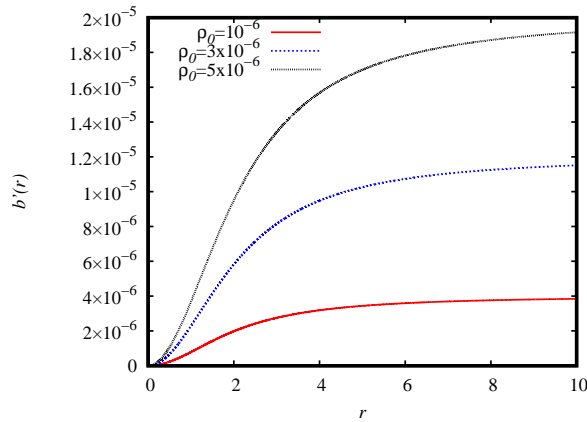


Figure 6: Behavior of $b'(r)$ considering the model (16) in terms of the radial coordinate with $r_0 = 1$, $R_s = 2$, and $\rho_c = 5 \times 10^{-5}$, for different values of ρ_0 . Changes in the density ρ_c do not significantly alter the shape of the graph.

B. Redshift function

From Eq. (1), (3), (13), and state equation $p(r) = \omega\rho(r)$, we find

$$e^{2\Phi(r)} = \left(\frac{r^2 + Rs^2}{r_0^2 + Rs^2} \right)^{\frac{2(1+2\omega)}{1+\omega}} \left[\frac{(r_0^2 + Rs^2)\rho_c - 2Rs^2\rho_0}{(r^2 + Rs^2)\rho_c - 2Rs^2\rho_0} \right]^2. \quad (17)$$

Once we have the shape function and the redshift function, we are able to calculate the Kretschmann scalar for the second model. However, as in the previous case, the analytical expression is not clear. An information we can extract from the analytical expression is that

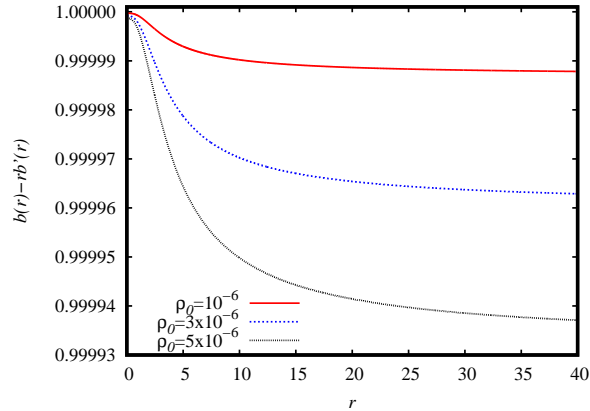


Figure 7: Behavior of $b(r) - rb'(r)$ considering the model (16) in terms of the radial coordinate with $r_0 = 1$, $R_s = 2$, and $\rho_c = 5 \times 10^{-5}$, for different values of ρ_0 . Changes in the density ρ_c do not significantly alter the shape of the graph.

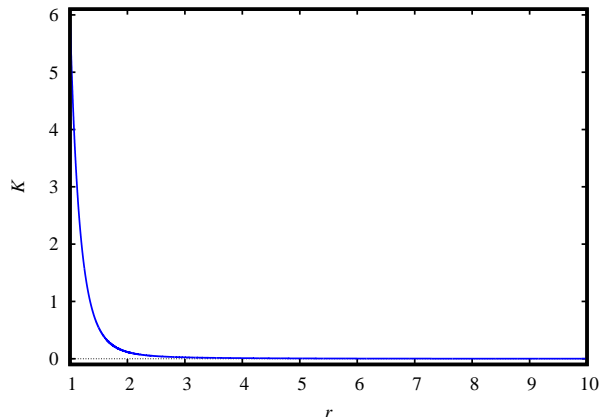


Figure 8: Behavior of the Kretschmann scalar for model (16), as a functions of the radial coordinate, with $\omega = 1$, $r_0 = 1$, $R_s = 2$, $\rho_c = 5 \times 10^{-6}$, and $\rho_0 = 10^{-6}$.

there are no singularities if $\rho_0 < \rho_c/2$. This limits the possible values of the dark matter energy density. In Fig. 8, we graphically observe the behavior of the Kretschmann scalar and see that it does not show divergences as it approaches the throat radius, decreasing to zero as the radial coordinate increases. As in the case before, parameter changes do not significantly alter the behavior of the Kretschmann scalar; therefore, we have not included additional curves in Fig. 8.

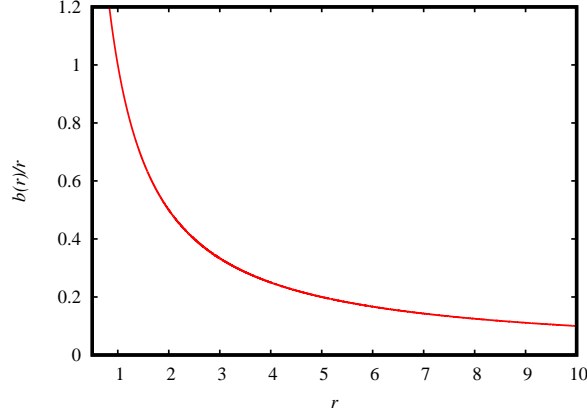


Figure 9: Behavior of $b(r)/r$ considering the model (18) in terms of the radial coordinate with $r_0 = 1$, $R_s = 2$, $\rho_c = 5 \times 10^{-5}$, and $\rho_0 = 10^{-7}$. Changes in the densities ρ_c and ρ_0 do not significantly alter the shape of the graph.

V. PF MODEL

A. Shape function

From Eqs. (1), (4), (7), and (10), we find that the corresponding wormhole shape function is given by

$$b(r) = r_0 - \frac{\rho_0^2 R_s^6}{3\rho_c r_0^3} + \frac{\rho_0^2 R_s^6}{3\rho_c r^3} + \rho_0 R_s^3 \log\left(\frac{r}{r_0}\right). \quad (18)$$

As in the previous cases, the condition $b(r_0) = r_0$ is identically satisfied since it was used in the integration to obtain $b(r)$. From Fig. 9, we see that $b(r)/r < 1$ for $r > r_0$, which satisfies the second condition for wormholes. In Fig. 10, we observe that $b' < 1$ at all points with different parameter values, which ensures that $b'(r_0) < 1$. Finally, in Fig. 11, we analyze the behavior of $b(r) - b'(r)r$ and verify that it is always positive for the chosen parameters. Thus, the wormhole that arises due to the dark matter profile 4 in LQC satisfies all the conditions imposed for wormholes.

B. Redshift function

From Eq. (1), (4), (13), and state equation $p(r) = \omega\rho(r)$, we find

$$e^{2\Phi(r)} = \left(\frac{r}{r_0}\right)^{\frac{6(1+2\omega)}{1+\omega}} \left(\frac{r_0^3 \rho_c - 2R_s^3 \rho_0}{r^3 \rho_c - 2R_s^3 \rho_0}\right)^2, \quad (19)$$

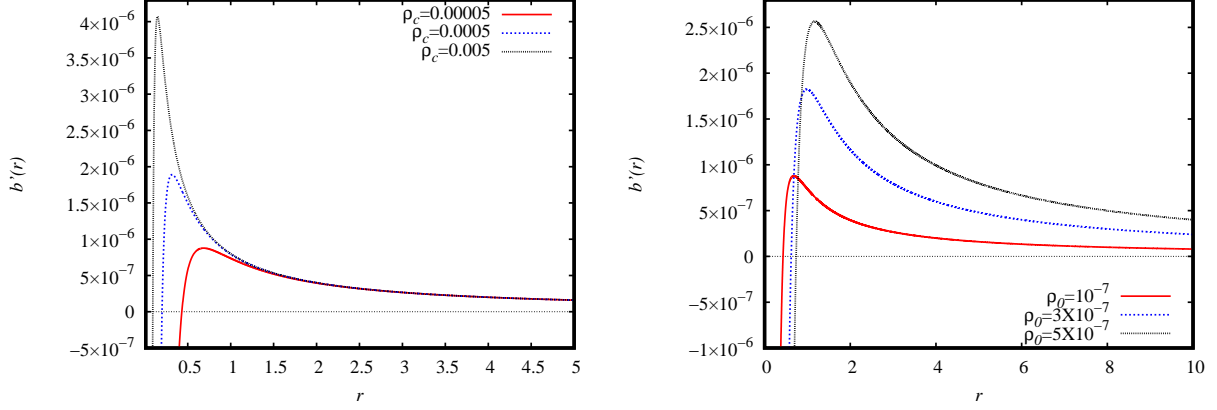


Figure 10: Behavior of $b'(r)$ considering the model (18) in terms of the radial coordinate with $r_0 = 1$ and $R_s = 2$. In the left panel, we fix $\rho_0 = 10^{-7}$ and vary ρ_c . In the right panel, we fix $\rho_c = 5 \times 10^{-5}$ and vary ρ_0 .

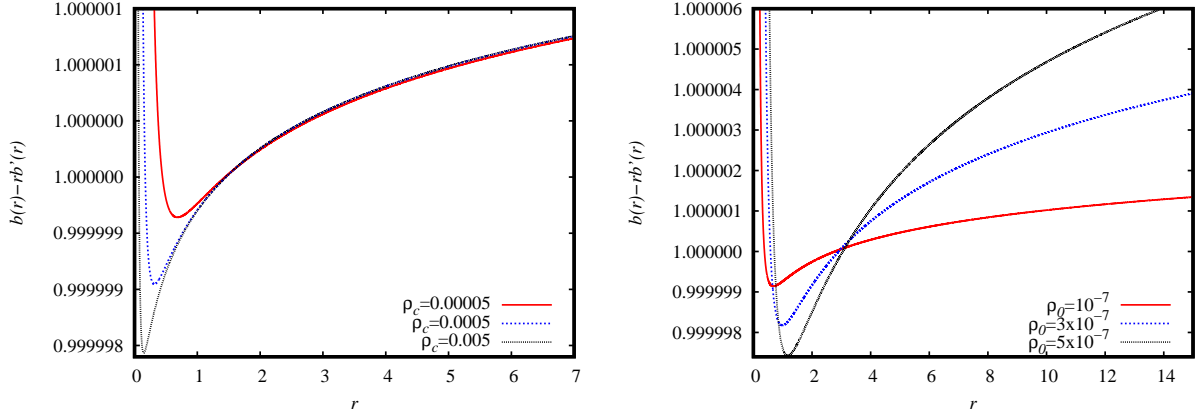


Figure 11: Behavior of $b(r) - rb'(r)$ considering the model (18) in terms of the radial coordinate with $r_0 = 1$ and $R_s = 2$. In the left panel, we fix $\rho_0 = 10^{-7}$ and vary ρ_c . In the right panel, we fix $\rho_c = 5 \times 10^{-5}$ and vary ρ_0 .

As in previous cases, we now have the necessary functions to calculate the Kretschmann scalar. Although the analytical expression is simpler than in previous cases, it is still quite confusing and unclear. Nevertheless, we can verify that, for our spacetime to be free of singularities, we need $\rho_0 < r_0^3 \rho_c / 2 R_s^3$. In Fig. 12, we graphically observe the behavior of the Kretschmann scalar and see that it does not show divergences as it approaches the throat radius, decreasing to zero as the radial coordinate increases. As in the cases before, parameter changes do not significantly alter the behavior of the Kretschmann scalar; therefore, we have not included additional curves in Fig. 12.

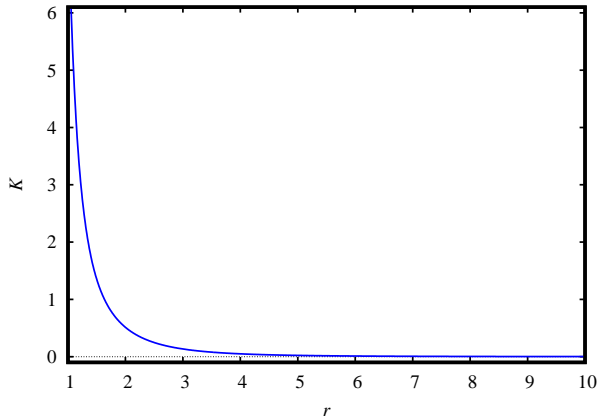


Figure 12: Behavior of the Kretschmann scalar for model (18), as a functions of the radial coordinate, with $\omega = 1$, $r_0 = 1$, $R_s = 2$, $\rho_c = 5 \times 10^{-5}$, and $\rho_0 = 10^{-7}$.

VI. EMBEDDING DIAGRAMS

In order to better analyze the shape of the wormholes we found, we will study the embedding diagrams. These type of diagrams help us to understand the curvature of the spacetime around compact objects, such as the wormholes.

To construct these diagrams, we will consider the line element that describes our wormhole models for the case $t = \text{constant}$ and considering the equatorial plane, $\theta = \pi/2$. With these simplifications, the line element is written as:

$$ds^2 = \frac{dr^2}{1 - \frac{b(r)}{r}} + r^2 d\phi^2. \quad (20)$$

Now, we will embed this spacetime into another spacetime, which is three-dimensional with cylindrical symmetry, assuming $\theta = \pi/2$. This three-dimensional spacetime is described by the line element:

$$ds_{cyl}^2 = d\rho^2 + \rho^2 d\phi^2 + dz^2. \quad (21)$$

Comparing the two line elements, we can identify:

$$\rho = r, \quad \text{and} \quad \frac{dz}{dr} = \pm \left(\frac{r}{b} - 1 \right)^{-1/2}. \quad (22)$$

Now, we just need to integrate equation (22) to obtain the shape of these wormholes to each model.

In Figs. 13 and 14, we show the behavior of the embedding diagram profile and the three-dimensional version of the diagrams for model (14). Depending on the chosen parameter

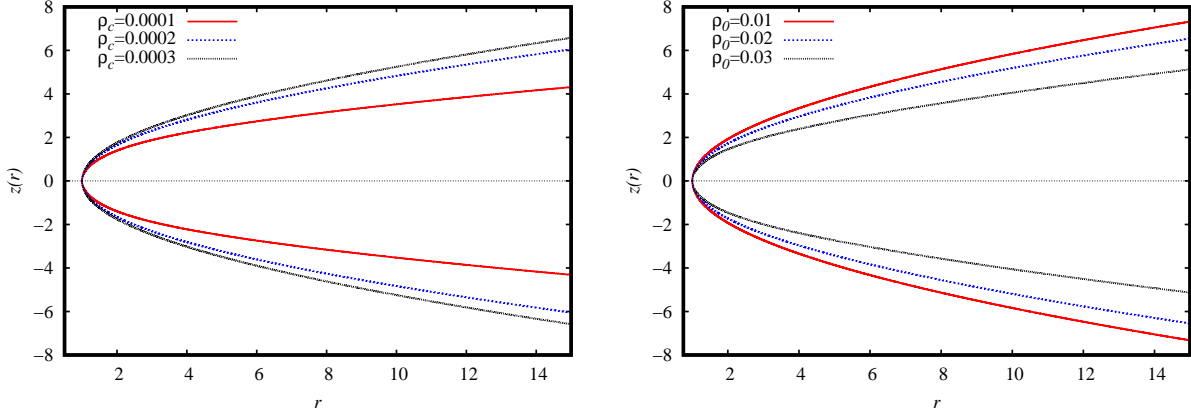


Figure 13: Behavior of $z(r)$ considering the model (14) in terms of the radial coordinate with $r_0 = 1$ and $R_s = 2$. In the left panel, we fix $\rho_0 = 0.01$ and vary ρ_c . In the right panel, we fix $\rho_c = 0.001$ and vary ρ_0 .

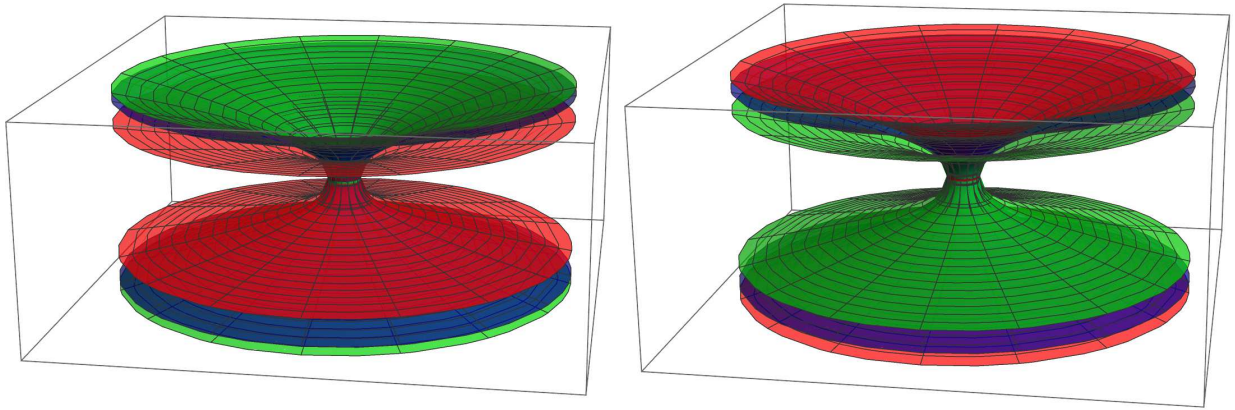


Figure 14: Embedding diagrams considering the model (14) in terms of the radial coordinate with $r_0 = 1$ and $R_s = 2$. In the left panel, we fix $\rho_0 = 0.01$ and consider $\rho_c = 0.0001$ (green), $\rho_c = 0.0002$ (blue), and $\rho_c = 0.0003$ (red). In the right panel, we fix $\rho_c = 0.001$ and consider $\rho_0 = 0.01$ (red), $\rho_0 = 0.02$ (blue), and $\rho_0 = 0.03$ (green).

values, the wormhole flattens more quickly. The higher the value of ρ_0 or the lower the value of ρ_c , the faster the wormhole flattens.

In Figs. 15 and 16, we show the behavior of the embedding diagram profile and the three-dimensional version of the diagrams for model (16). The behavior is similar to the first model, where the higher the value of ρ_0 or the lower the value of ρ_c , the faster the solution flattens. It is interesting to note that for larger values of ρ_c , the shape of the wormhole does not change much when ρ_c is further increased.

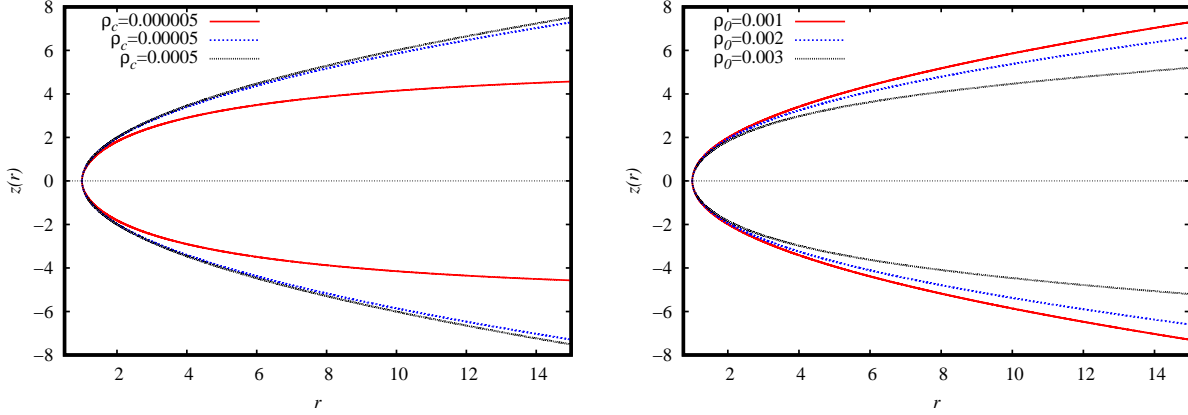


Figure 15: Behavior of $z(r)$ considering the model (16) in terms of the radial coordinate with $r_0 = 1$ and $R_s = 2$. In the left panel, we fix $\rho_0 = 0.001$ and vary ρ_c . In the right panel, we fix $\rho_c = 0.00005$ and vary ρ_0 .

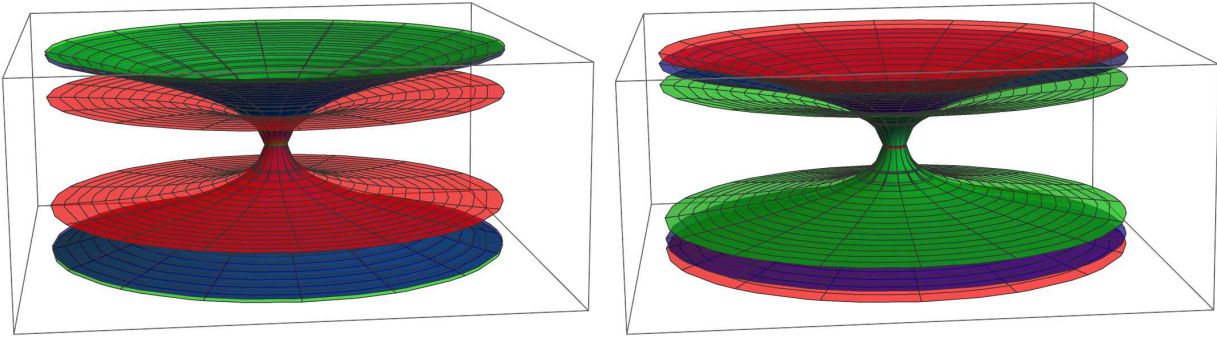


Figure 16: Embedding diagrams considering the model (16) in terms of the radial coordinate with $r_0 = 1$ and $R_s = 2$. In the left panel, we fix $\rho_0 = 0.001$ and consider $\rho_c = 0.000005$ (green), $\rho_c = 0.00005$ (blue), and $\rho_c = 0.0005$ (red). In the right panel, we fix $\rho_c = 0.00005$ and consider $\rho_0 = 0.001$ (red), $\rho_0 = 0.002$ (blue), and $\rho_0 = 0.003$ (green).

Finally, 17 and 18, we show the behavior of the embedding diagram profile and the three-dimensional version of the diagrams for model (18). The behavior is similar to the first model, where the higher the value of ρ_0 or the lower the value of ρ_c , the faster the solution flattens. Thus, even though the shape function of each wormhole is completely different, graphically the behavior of the wormhole shape for each dark matter profile is quite similar.

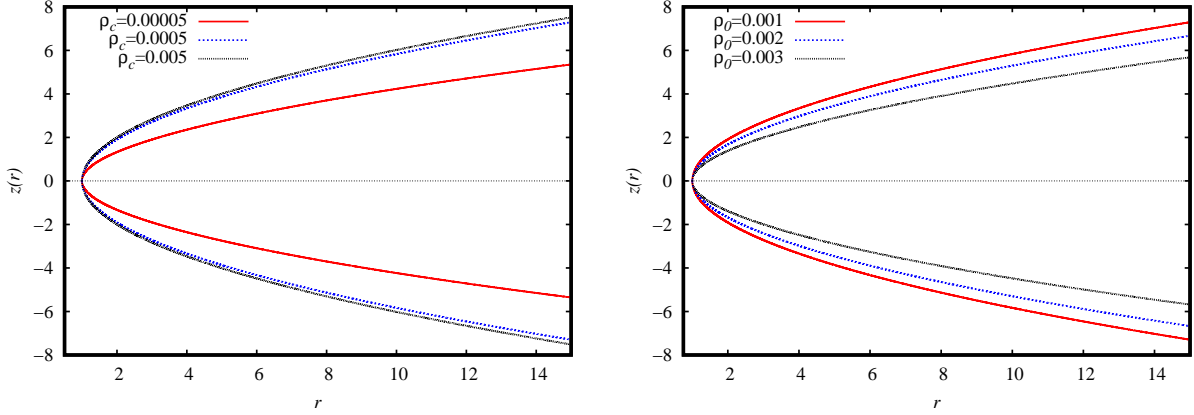


Figure 17: Behavior of $z(r)$ considering the model (18) in terms of the radial coordinate with $r_0 = 1$ and $R_s = 2$. In the left panel, we fix $\rho_0 = 0.001$ and vary ρ_c . In the right panel, we fix $\rho_c = 0.0005$ and vary ρ_0 .

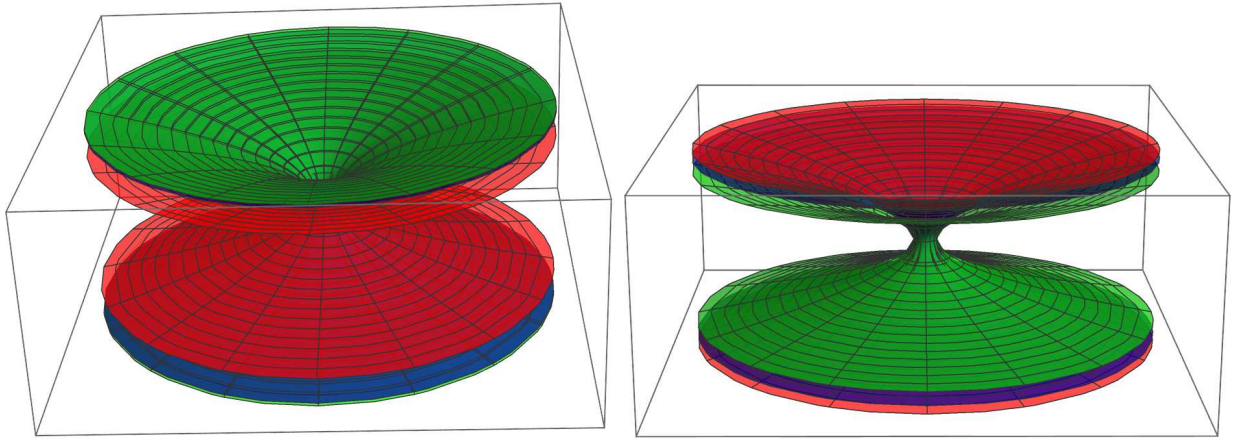


Figure 18: Embedding diagrams considering the model (18) in terms of the radial coordinate with $r_0 = 1$ and $R_s = 2$. In the left panel, we fix $\rho_0 = 0.001$ and consider $\rho_c = 0.00005$ (green), $\rho_c = 0.0005$ (blue), and $\rho_c = 0.005$ (red). In the right panel, we fix $\rho_c = 0.0005$ and consider $\rho_0 = 0.001$ (red), $\rho_0 = 0.002$ (blue), and $\rho_0 = 0.003$ (green).

VII. ENERGY CONDITIONS AND QUANTITY OF EXOTIC MATTER

The energy conditions are constraints imposed on the components of a given stress-energy tensor to ensure its physical viability. In the case of wormholes, the violation of certain energy conditions is essential to keep the wormhole's throat traversable.

To our case, let's consider the components of the stress-energy tensor given by (6). The

energy conditions are given by the inequalities:

$$NEC = WEC_1 = SEC_1 \iff \rho_e + p_e \geq 0, \quad (23)$$

$$SEC_2 \iff \rho_e + 3p_e \geq 0, \quad (24)$$

$$DEC_1 \iff \rho_e - |p_e| \geq 0 \iff (\rho_e + p_e \geq 0) \text{ and } (\rho_e - p_e \geq 0), \quad (25)$$

$$DEC_2 = WEC_2 \iff \rho_e \geq 0, \quad (26)$$

where the energy conditions are the null (NEC), weak (WEC), strong (SEC), and dominant (DEC). We see that the NEC is embedded within the other conditions. Thus, if the NEC is violated, the other conditions will also be violated. However, the reverse is not necessarily true, as the other conditions also impose additional inequalities that do not appear in the NEC. Now let's analyze the conditions for each dark matter model.

In this section, we will also analyze the quantity of exotic matter necessary to maintain the wormhole by calculating the Volume Integral Quantifier (VIQ), defined by [31]

$$\mathcal{I}_v = \int_{r_0}^r 4\pi x^2 (\rho_e + p_e) dx, \quad (27)$$

where $r \rightarrow \infty$. We will perform this calculation for the three dark matter models considered up to this point.

A. NFW model

Considering the model (2), we can calculate the components of the stress-energy tensor, and we obtain that their combinations are given by:

$$\rho_e + p_e = \frac{\rho_0 R_s^3 (\omega + 1) (r \rho_c (r + R_s)^2 - 2\rho_0 R_s^3)}{\rho_c r^2 (r + R_s)^4}, \quad (28)$$

$$\rho_e + 3p_e = \frac{\rho_0 R_s^3 (r \rho_c (r + R_s)^2 (3\omega + 1) - 2\rho_0 R_s^3 (3\omega + 2))}{\rho_c r^2 (r + R_s)^4}, \quad (29)$$

$$\rho_e - p_e = \frac{\rho_0 R_s^3 (r \rho_c (r + R_s)^2 (1 - \omega) + 2\rho_0 R_s^3 \omega)}{\rho_c r^2 (r + R_s)^4}, \quad (30)$$

$$\rho_e = \frac{\rho_0 R_s^3 (\rho_c r (r + R_s)^2 - \rho_0 R_s^3)}{\rho_c r^2 (r + R_s)^4}. \quad (31)$$

Analyzing Eq. (28), we notice that, for $\omega > -1$, NEC will be violated for small values of the radial coordinate. This violation can be mitigated by increasing the value of ρ_c or decreasing the value of ρ_0 . As long as $\omega > -1$, the value of ω will not affect the region

where NEC is satisfied. If $\omega < -1$, the regions where NEC was previously satisfied will now be violated, and where it was violated, it will now be satisfied. Through Eq. (29), we see that if $\omega > -\frac{1}{3}$, the relation $\rho_e + 3p_e$ will be positive for regions farther from the wormhole, thus the SEC will be violated in more central regions. For $-\frac{1}{3} \geq \omega \geq -\frac{2}{3}$, the SEC will always be violated. Finally, for $\omega < -\frac{2}{3}$, the SEC will be violated in more distant regions and satisfied in regions closer to the wormhole. From Eq. (30), we see that for $\omega \leq 1$, the relation $\rho_e - p_e$ will always be positive. This ensures that at least one of the inequalities of DEC will always be satisfied. If $\omega > 1$, the relation will be negative for points farther from the wormhole and positive in more central regions. The region where this inequality will be violated depends on the value of ω ; the larger ω is, the larger the region where the DEC will be violated. The behavior of Eq. (31) is similar to that of Eq. (28). The density ρ_e will be negative for small values of the radial coordinate and positive for points farther from the wormhole. This means that one of the inequalities of the WEC will not be satisfied in more central regions. This violation can be mitigated by increasing ρ_c or decreasing the values of ρ_0 .

The quantity of exotic matter for the NFW model, calculated via Eq. (27) yields

$$\begin{aligned} \mathcal{I}_v = & 4\pi R_s^3(1+w)\frac{\rho_0}{\rho_c} \left[\frac{2}{3}R_s^3 \left(\frac{1}{(r+R_s)^3} - \frac{1}{(r_0+R_s)^3} \right) \rho_0 + R_s \left(\frac{1}{(r+R_s)} - \frac{1}{(r_0+R_s)} \right) \rho_c \right. \\ & \left. + \rho_c \log \left(\frac{r+R_s}{r_0+R_s} \right) \right]. \end{aligned} \quad (32)$$

In the limit $r \gg R_s$, we have $\mathcal{I}_v \approx 4\pi\rho_0 R_s^3(\omega+1)\log\left(\frac{r}{r_0+R_s}\right)$. Then, when $r \rightarrow \infty$ the integral diverges logarithmically. However, for $\omega \rightarrow -1$ this quantity vanishes.

B. PI model

Considering the model (3), we can calculate the components of the stress-energy tensor, and we obtain that their combinations are given by:

$$\rho_e + p_e = \frac{\rho_0 R_s^2 (\omega + 1) (R_s^2 (\rho_c - 2\rho_0) + \rho_c r^2)}{\rho_c (r^2 + R_s^2)^2}, \quad (33)$$

$$\rho_e + 3p_e = \frac{\rho_0 R_s^2 (\rho_c r^2 (3\omega + 1) + R_s^2 (-2\rho_0 (3\omega + 2) + \rho_c (3\omega + 1)))}{\rho_c (r^2 + R_s^2)^2}, \quad (34)$$

$$\rho_e - p_e = \frac{\rho_0 R_s^2 \rho_c ((r^2 + R_s^2)(1 - \omega) + 2R_s^2 \rho_0 \omega)}{\rho_c (r^2 + R_s^2)^2}, \quad (35)$$

$$\rho_e = \frac{\rho_0 R_s^2 (\rho_c r^2 + R_s^2 (\rho_c - \rho_0))}{\rho_c (r^2 + R_s^2)^2}. \quad (36)$$

For $\omega = -1$, the NEC is identically satisfied, since Eq. (33) would be null in this case. For $\omega > -1$, NEC will always be satisfied if $\rho_c \geq 2\rho_0$. If $\rho_c < 2\rho_0$, NEC will be violated near the center of the wormhole. This violation will be mitigated the smaller ρ_0 is or the larger ρ_c is. For $\rho_c > 2\rho_0(3\omega + 2)/(3\omega + 1)$, the relation $\rho_e + 3p_e$, Eq. (34), will always be positive, thus satisfying SEC. If $\omega < 1$, the relation $\rho_e - p_e$, Eq. (35), will always be positive, satisfying DEC. For $\omega > 1$, DEC will be satisfied in more internal regions and violated at points farther from the wormhole. If $\rho_c > \rho_0$, Eq. (36), the energy density ρ_e will always be positive, contributing to NEC being always satisfied.

The quantity of exotic matter at r for the PI model is given by

$$\begin{aligned} \mathcal{I}_v = & 4\pi R_s^2 (1 + \omega) \frac{\rho_0}{\rho_c} \left[r R_s^2 \rho_0 \left(\frac{1}{r^2 + R_s^2} - \frac{1}{r_0^2 + R_s^2} \right) + (r - r_0) \rho_c \right. \\ & \left. - R_s (\rho_0 + \rho_c) \left(\tan^{-1} \left(\frac{r}{R_s} \right) - \tan^{-1} \left(\frac{r_0}{R_s} \right) \right) \right], \end{aligned} \quad (37)$$

and for $r \ll R_s$, $\mathcal{I}_v \approx 4\pi R_s^2 \rho_0 (1 + \omega) r$, diverging, therefore, linearly with r . Once more, the quantifier vanishes for $\omega \rightarrow -1$.

C. PF model

Considering the model (4), we can calculate the components of the stress-energy tensor, and we obtain that their combinations are given by:

$$\rho_e + p_e = \frac{\rho_0 R_s^3 (\omega + 1) (\rho_c r^3 - 2\rho_0 R_s^3)}{\rho_c r^6}, \quad (38)$$

$$\rho_e + 3p_e = \frac{\rho_0 R_s^3 (\rho_c r^3 (3\omega + 1) - 2\rho_0 R_s^3 (3\omega + 2))}{\rho_c r^6}, \quad (39)$$

$$\rho_e - p_e = \frac{\rho_0 R_s^3 (r^3 \rho_c (1 - \omega) + 2\rho_0 R_s^3 \omega)}{\rho_c r^6}, \quad (40)$$

$$\rho_e = \frac{\rho_0 R_s^3 (\rho_c r^3 - \rho_0 R_s^3)}{\rho_c r^6}. \quad (41)$$

For $\omega > -1$, the combination $\rho_e + p_e$, Eq. (38), will present positive values for $r > \sqrt[3]{2\rho_0/\rho_c} R_s$. Therefore, NEC will only be violated in the region $r < \sqrt[3]{2\rho_0/\rho_c} R_s$. For the case where $\omega < -1$, NEC will be violated for $r > \sqrt[3]{2\rho_0/\rho_c} R_s$. If $\omega = -1$, NEC will be identically satisfied in all regions. For $\omega > -\frac{1}{3}$, the combination $\rho_e + 3p_e$, Eq. (39), is negative for small values of r . Thus, SEC is violated in this region, and this violation can be mitigated by increasing ρ_c or decreasing ρ_0 . For $-\frac{1}{3} \geq \omega > -\frac{2}{3}$, SEC will always be violated. For $\omega < -\frac{2}{3}$, SEC will be violated at points farther from the wormhole, with this violation being mitigated by increasing ρ_0 or decreasing ρ_c . For $\omega \leq 1$, the combination $\rho_e - p_e$, (40), will always be positive, so the DEC will always be satisfied. For $\omega > 1$, the DEC will be violated in regions farther from the wormhole. For $r > \sqrt[3]{\rho_0/\rho_c} R_s$, the energy density ρ_e is always positive, so WEC will be violated in regions where $r < \sqrt[3]{\rho_0/\rho_c} R_s$.

For the PF dark matter model, the quantifier of exotic dark matter is

$$\mathcal{I}_v = 4\pi R_s^3 (1 + \omega) \frac{\rho_0}{\rho_c} \left[\frac{2R_s^3 \rho_0}{3} \left(\frac{1}{r^3} - \frac{1}{r_0^3} \right) + \rho_c \log \left(\frac{r}{r_0} \right) \right], \quad (42)$$

which also diverges logarithmically for $r \rightarrow \infty$ and vanishes for $\omega \rightarrow -1$.

In Figure 19, we show VIQ as a function of the radial coordinate for the three models, each evaluated at two different values of ρ_c . Notice that as this latter decreases, the quantity of exotic matter reduces across all models, with the PF model exhibiting the most significant reduction. Overall, the PI model requires the largest amount of exotic matter, while the NFW model requires the least.

In LQC, a lower critical density ρ_c introduces quantum gravitational effects at lower densities, reducing the need for exotic matter to sustain non-standard spacetime structures.

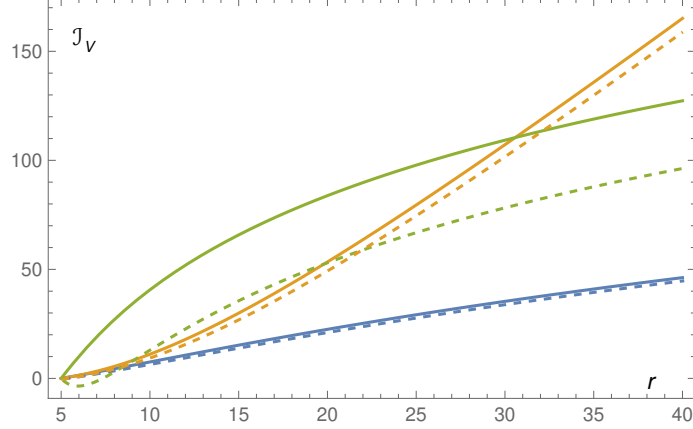


Figure 19: VIQ as a function of the radial coordinate, for the NFW model, in blue and dashed blue, for PI model, in green and dashed green, and for PF model, in orange and dashed orange. The set parameters are $\rho_c = 1.0$ (solid curves), $\rho_c = 0.1$ (dashed curves), $\rho_0 = 0.01$, $r_0 = 5.0$, $\omega = -1/2$, and $R_s = 10.0$.

Additionally, quantum corrections impact spacetime at larger radial distances, stabilizing structures like wormholes without as much exotic matter. Thus, a reduced ρ_c shifts the balance, allowing quantum geometry to fulfill part of the role typically assigned to exotic dark matter.

VIII. SOLUTION STABILITY

In this section we evaluate the stability of the obtained wormhole solutions through the analysis of the radial sound velocity within the dark matter fluid [32]. This quantity, denoted as $(v_s)^2$, can be calculated as follows:

$$(v_s)^2 = \frac{dp_e}{d\rho_e} = \frac{dp_e/dr}{d\rho_e/dr}. \quad (43)$$

Wormhole stability is ensured if $v_s^2 > 0$, with the condition $v_s < 1$ required to maintain subluminal velocities. Our analysis focuses on the throat at $r = r_0$.

In left panel of Figure 20, we illustrate the parameter space (ρ_c, ω) for various values of the critical dark matter density ρ_0 , with other parameters held constant. Although the plot describes the stability and physicality of the NFW model, the behavior is similar in the other dark matter models. Notably, a lower concentration of ρ_0 expands (reduces) the regions where stability and physical viability are achieved, particularly for $\omega > 0$ ($\omega < 0$).

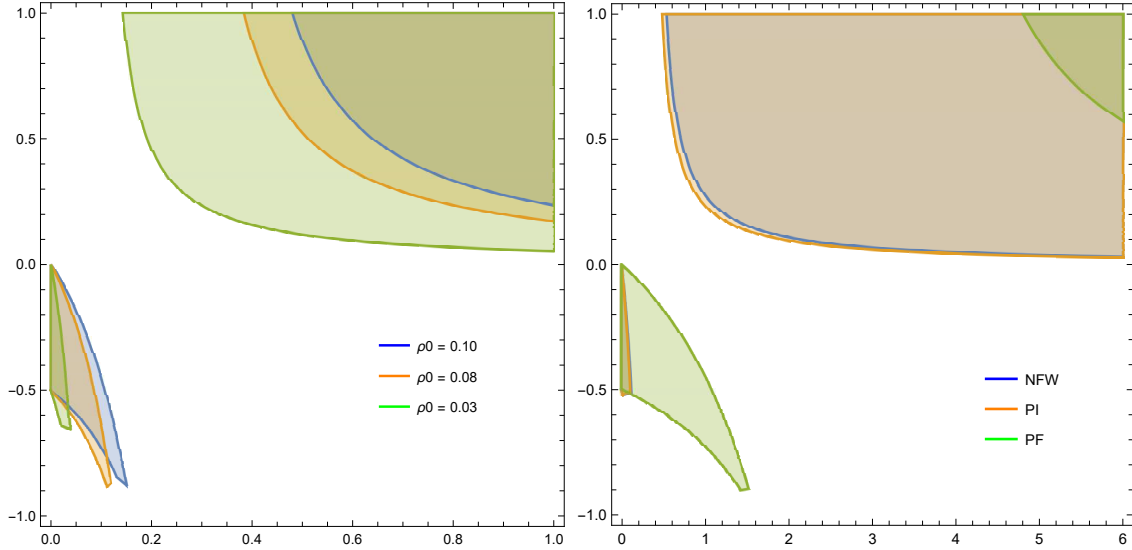


Figure 20: Left panel: Parameter space (ρ_c, ω) for the NFW model, identifying regions at the throat where wormhole solutions exhibit stability and physical viability, namely where $0 < v_s^2 < 1$, for selected values of ρ_0 , with $r_0 = 5.0$ and $R_s = 10.0$ held constant. Right panel: Comparison between the parameter spaces of the three models, for $\rho_0 = 0.1$ and same values for the other parameters.

Conversely, higher values of ρ_0 reduce (expand) these regions. We also observe that as the solutions become classical (*i.e.*, non-quantum, $\rho_c \rightarrow \infty$), the dark matter-sourced wormhole solutions tend to the stability, particularly for $\omega \geq 0$.

In the right panel of the same figure, we compare the stability and physicality regions across the parameter spaces of the three models. Notably, the PI model exhibits the largest parameter space for $\omega > 0$, while the PF model shows the largest region for $\omega < 0$. In other words, the PF model favors an exotic, quantum nature of dark matter in scenarios where non-classical effects ($\rho_c \rightarrow 0$) become more significant.

IX. CONCLUSIONS

In this paper, we obtain wormhole solutions in the context of LQC. As a source of matter, we chose three different dark matter profiles that are well-known and studied in the literature. To obtain these solutions, we solved the field equations of LQC and the conservation equation for the energy-momentum tensor, with the appropriate boundary conditions. It was also necessary to choose an equation of state, for which we adopted

$p = \omega\rho$. So that, we obtained the appropriate expressions for the shape function, $b(r)$, and the redshift function, $\Phi(r)$.

Even though it was obtained through the boundary conditions for a wormhole, it was still necessary to verify whether the shape function satisfied certain criteria. We thus found that all models satisfy the established criteria for wormholes. Furthermore, we found that for these spacetimes to be regular, the energy density of dark matter, ρ_0 , needed to have a maximum limit, with each model having a different limit. Once the criteria for the regularity of the spacetimes were established, we verified through the Kretschmann scalar plots that there were no singularities in our spacetimes.

Through the embedding diagrams, we were able to visualize the structure of these wormholes. We verified that the smaller the value of ρ_c or the larger the value of ρ_0 , the faster these wormholes flatten out. The embedding diagrams also allowed us to visualize that there is a minimum radius, which is precisely the throat radius of the wormholes.

We studied the energy conditions for all models. If $\omega = -1$, the null energy condition is identically satisfied for all models. For $\omega \neq -1$, models (2) and (4) always violate the null energy condition in the innermost regions of the wormhole, equations (28) and (38). For the second model, if $\rho_c \geq 2\rho_0$, the null condition will always be satisfied, while for $\rho_c < 2\rho_0$, the null condition will be violated in more central regions, equation (33). In models (2) and (4), the energy densities will always have negative values in central regions, equations (31) and (41). In model (3), if $\rho_c \geq \rho_0$, the density will be positive at all points, equation (36). The second model satisfies the energy conditions with fewer restrictions than the other cases.

We further investigated the amount of exotic matter required to stabilize the wormholes by calculating the volume integral quantifier (VIQ), \mathcal{I}_v . Our findings suggest that, across the three analyzed models, a smaller amount of exotic dark matter is generally required as quantum effects intensify (i.e., for lower values of the critical density, ρ_c), with this effect being particularly notable in the PF model. Overall, the PI model requires the largest amount of exotic matter, while the NFW model requires the least. However, near the throat, the PF model demands the highest amount of exotic matter, as shown in the plot in Figure 19.

Finally, we analyzed the stability of the wormhole solutions at the throat by computing the sound velocity within the isotropic fluid and identifying the regions in the parameter space (ρ_c, ω) where $0 \leq v_s \leq 1$. Our results show that the PI model, followed by the NFW

model, offers a broader range of conditions to ensure both stability and physical viability for $\omega > 0$. Conversely, the PF model exhibits the most robust stability conditions for $\omega < 0$.

In conclusion, we have demonstrated that various dark matter profiles in Loop Quantum Cosmology lead to stable, regular traversable wormhole solutions, with our results highlighting the substantial impact of quantum effects on wormhole structure. This work lays the groundwork for further investigation into dark matter's role in supporting exotic geometries within quantum gravity frameworks.

Acknowledgments

The authors would like to thank Fundação Cearense de Apoio ao Desenvolvimento Científico e Tecnológico (FUNCAP) for partial financial support. CRM thanks the Conselho Nacional de Desenvolvimento Científico e Tecnológico (CNPq), Grants no. 308268/2021-6.

-
- [1] B. P. Abbott *et al.*, collaboration LIGO Scientific, Virgo, Phys. Rev. Lett. **116**, 6, 061102 (2016).
 - [2] A. Einstein and N. Rosen, Phys. Rev. **48**, 73-77 (1935).
 - [3] M. S. Morris and K. S. Thorne, Am. J. Phys. **56**, 395-412 (1988).
 - [4] S. W. Hawking, Phys. Rev. D **37**, 904-910 (1988).
 - [5] M. Visser, “Lorentzian wormholes: From Einstein to Hawking”, ISBN 978-1-56396-653-8 (1995).
 - [6] k. k. Nandi, Y-Z Zhang, and k. b. v. Kumar, Phys. Rev. **70**, 127503 (2004).
 - [7] M. S. Churilova, R. A. Konoplya, Z. Stuchlik and A. Zhidenko, JCAP **10** (2021), 010.
 - [8] R. A. Konoplya and A. Zhidenko, Phys. Rev. Lett. **128** (2022) no.9, 091104.
 - [9] A. Ashtekar, J. Phys. Conf. Ser. **189**, 012003 (2009).
 - [10] R. Sengupta, S. Ghosh, and M. Kalam, Eur. Phys. J. **C83**, 9, 830 (2023).
 - [11] C. R. Muniz, T. Tangphati, R. M. P. Neves, and M. B. Cruz, Phys. Dark Univ. **46**, 101673 (2024).
 - [12] N. Aghanim *et al.*, A& A **641**, A6 (2020).
 - [13] F. Zwicky, Fritz, Helv. Phys. Acta, **6**, 110 (1933).

- [14] V. C. Rubin, Jr. Ford, Jr., W. Kent, *Astrophys. J.* **159**, 379–403 (1970).
- [15] G. Bertone and D. Hooper, *Rev.Mod.Phys.* **90**, 4, 045002 (2018).
- [16] M. Persic, P. Salucci, and F. Stel, *Mont. N. R. Astr. Soc.*, **281**, 1, 27 (1996).
- [17] L. Randall, *Nature* **557**, S6-S7 (2018).
- [18] C.A. Argüeles *et al.*, *Rev. Mod. Phys.* **93**, 035007 (2021).
- [19] D. J. E. Marsh, D. Ellis, and V. M. Mehta, “Dark Matter: Evidence, Theory, and Constraints”, ISBN 978-0-691-24952-0, Princeton University Press, Sept. (2024).
- [20] C. R. Muniz, and R. V. Maluf, *Annals Phys.* **446**, 169129 (2022).
- [21] Z. Xu, Zhaoyi, M. Tang, G. Cao, and S-N. Zhang, *Eur. Phys. J.* **C80**, 1, 70 (2020).
- [22] G. Mustafa, S. K. Maurya, and S. Ray, *Fortsch. Phys.* **71**, 6-7, 2200129 (2023).
- [23] R. Radhakrishnan *et al.*, *Symmetry* **16**, 8, 1007 (2024).
- [24] A. Errehymy *et al.*, *Eur. Phys. J.* **C84**, 6, 573 (2024).
- [25] S. K. Maurya, J. Kumar, S. Kiroriwal, and A. Errehymy, *Phys. Dark Univ.*, **46**, 101564 (2024).
- [26] Z. Hassan and P. K. Sahoo, *Annalen Phys.* **536**, 8, 2400114, (2024).
- [27] J. F. Navarro, C. S. Frenk, and S. D. M. White, *Astrophys. J* **462**, 563–575 (1996).
- [28] M-H. Li and K. C. Yang, *Phys. Rev.* **D86**, 123015 (2012).
- [29] A. Ashraf, F. Javed, W-X. Ma, and A. Waseem, *Eur. Phys. J. Plus* **139**, 9, 857 (2024).
- [30] K. G. Begeman, A. H. Broeils, and R. h. Sanders, *Mon. Not. Roy. Astron. Soc.* **249**, 523 (1991).
- [31] K. K. Nandi, Y. Z. Zhang and K. B. Kumar, *Phys. Rev. D* **70**, 127503 (2004).
- [32] S. Capozziello and N. Godani, *Phys. Lett.* **B835**, 137572 (2022).